Perspectives on Clustering and Declustering of Earthquakes

Ilya Zaliapin*[1] and Yehuda Ben-Zion[2]

Abstract

Clustering is a fundamental feature of earthquakes that impacts basic and applied analyses of seismicity. Events included in the existing short-duration instrumental catalogs are concentrated strongly within a very small fraction of the space–time volume, which is highly amplified by activity associated with the largest recorded events. The earthquakes that are included in instrumental catalogs are unlikely to be fully representative of the long-term behavior of regional seismicity. We illustrate this and other aspects of space–time earthquake clustering, and propose a quantitative clustering measure based on the receiver operating characteristic diagram. The proposed approach allows eliminating effects of marginal space and time inhomogeneities related to the geometry of the fault network and regionwide changes in earthquake rates, and quantifying coupled space–time variations that include aftershocks, swarms, and other forms of clusters. The proposed measure is used to quantify and compare earthquake clustering in southern California, western United States, central and eastern United States, Alaska, Japan, and epidemic-type aftershock sequence model results. All examined cases show a high degree of coupled space–time clustering, with the marginal space clustering dominating the marginal time clustering. Declustering earthquake catalogs can help clarify long-term aspects of regional seismicity and increase the signal-to-noise ratio of effects that are subtler than the strong clustering signatures. We illustrate how the high coupled space–time clustering can be decreased or removed using a data-adaptive parsimonious nearest-neighbor declustering approach, and emphasize basic unresolved issues on the proper outcome and quality metrics of declustering. At present, declustering remains an exploratory tool, rather than a rigorous optimization problem, and selecting an appropriate declustering method should depend on the data and problem at hand.

Cite this article as Zaliapin, I., and Y. Ben-Zion (2021). Perspectives on Clustering and Declustering of Earthquakes, *Seismol. Res. Lett.* **93**, 386–401, doi: 10.1785/0220210127.

Supplemental Material

Introduction

Earthquake clustering is a fundamental aspect of seismicity. It is manifested most clearly by concentration of seismicity around tectonic plate boundaries and large faults (spatial clustering; see Figs. 1a and 2a) and after large earthquakes (aftershocks; see Figs. 1b and 2b), and is also associated with foreshocks, swarms, and other types of linked events (e.g., Jones and Molnar, 1979; Kagan and Jackson, 1991; Press and Allen, 1995; Utsu, 2002; Ben-Zion, 2008; Mignan, 2014; Zaliapin and Ben-Zion, 2016; Ross and Cochran, 2021). Earthquake clustering reflects various forms of triggering mechanisms, including static and dynamic stress transfers from previous earthquakes, fluid migration, and aseismic slip below and along faults (e.g., Dieterich, 1994; Console *et al.*, 2006; Felzer and Brodsky, 2006; Lengliné *et al.*, 2012; Ross *et al.*, 2017; Kato and Ben-Zion, 2021). On one hand, clustering of seismicity is important for many purposes such as identifying the character and interaction of active fault structures (e.g., Ruhl *et al.*, 2016), estimating time-dependent distribution of earthquakes (e.g., Ogata, 1999; Field *et al.*, 2017), and more. On the other hand, efforts to clarify less obvious aspects of earthquake dynamics benefit from using declustered catalogs that do not include aftershocks, foreshocks, and other strong forms of clustering. Examples include detection of tidal, seasonal, hydrologic, climatic, and anthropogenic triggering of seismicity (e.g., Cochran *et al.*, 2004; Amos *et al.*, 2014; Goebel and Brodsky, 2018; Hammond *et al.*, 2019; Johnson *et al.*, 2019; Hsu *et al.*, 2021). For some applications, it is also important to consider the "background" earthquake activity, generated within a given volume by the long-term regional

1. Department of Mathematics and Statistics, University of Nevada, Reno, Reno, Nevada, U.S.A., https://orcid.org/0000-0001-6257-0517 (IZ); 2. Department of Earth Sciences, Southern California Earthquake Center, Zumberge Hall of Science, University of Southern California, Los Angeles, California, U.S.A.

*Corresponding author: zal@unr.edu

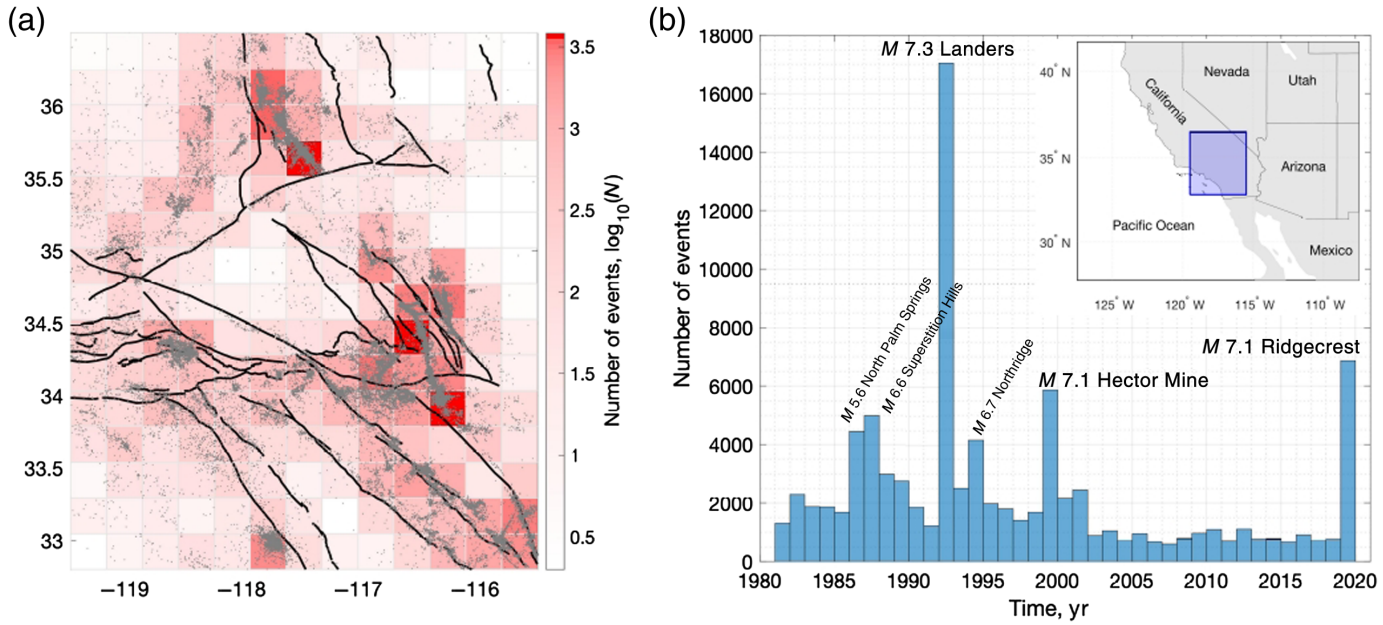

Figure 1. Spatiotemporal clustering of earthquakes in southern California based on the catalog of Hauksson *et al.* (2012, extended) for the period 1981–2020. (a) Map view of earthquakes with $M \geq 2$ (gray). Shades of red color reflect the number of events (logarithmic scale; see color bar) in each square spatial cell with the side length equal to 0.25° latitude. Black lines show major faults. The most active cell at 116.4° W, 33.7° N with 3822 events covers the aftershock sequence of 1992 M 7.3 Landers earthquake. (b) Event counts in 1 yr time intervals. The largest counts correspond to the most numerous aftershock sequences (marked in the figure). (Inset) The location of the examined region (blue rectangle). The color version of this figure is available only in the electronic edition.

tectonic processes, separated from the chains of triggered seismicity that typically follow the background events. Examples include development of long-term seismic hazard maps (e.g., Petersen *et al.*, 2015, 2018), inversions of focal mechanisms for the background stress field operating on the volume under consideration (e.g., Martínez-Garzón *et al.*, 2016; Abolfathian *et al.*, 2019), and estimations of evolving localization of seismicity before large earthquakes (e.g., Ben-Zion and Zaliapin, 2020).

The duration of instrumental earthquake catalogs is very short (typically only a few tens of years) relative to the duration of large earthquake cycles. Accordingly, the available catalogs are often dominated by aftershocks of the largest earthquakes that happened to occur during the observational period. The instrumental catalogs may also be influenced by aftershocks of nonrecorded historical events and aftershocks of events outside of the examined spatial region (Wang, Jackson, and Zhuang, 2010; van der Elst, 2017). As a result, the recorded activity is not necessarily representative of what might occur in the following 20 yr (or even 5 yr). The strong clustering of seismicity masks other properties and reduces the ability to understand other phenomena and the long-term large-scale dynamics of earthquakes for which local triggering effects are averaged out.

A high degree of earthquake clustering is commonly obscured (quite deceivingly) by a strong space–time concentration that is not easily discernible in a visual catalog inspection. Several key clustering phenomena are described by power laws that apply to earthquake size (e.g., frequency-moment statistics related to the Gutenberg–Richter law), time (e.g., Omori law), and location (e.g., decay of seismic rate with distance from the fault core); see Ben-Zion (2008, table 2) for details and further examples. The intermediate portions of these power laws are well established observationally, but the tails associated with small-scale (left tails) and large-scale (right tails) features remain underexplored. Most relevant for the present article are the left tails and the fact that the majority of events in the available catalogs occur within a tiny fraction of the total examined space–time volume in the immediate vicinity of other events, in accordance with the Omori–Utsu power-law temporal decay of aftershock sequences (Utsu and Ogata, 1995) and the power-law decay of seismic intensity off the fault core (Felzer and Brodsky, 2006; Dieterich and Smith, 2009; Powers and Jordan, 2010; Goebel *et al.*, 2014). Although these laws are well known, the severity of their consequences for earthquake clustering is rarely quantified, and the effects of such clustering remain underappreciated. In the following sections, we illustrate and quantify earthquake clustering with examples of seismicity from southern California and other regions. We propose a simple and robust measure of space–time clustering (G) that allows disentangling effects related to concentration of events around a heterogeneous fault network from additional coupled space–time fluctuations. We show that the observed catalogs are dominated by the marginal

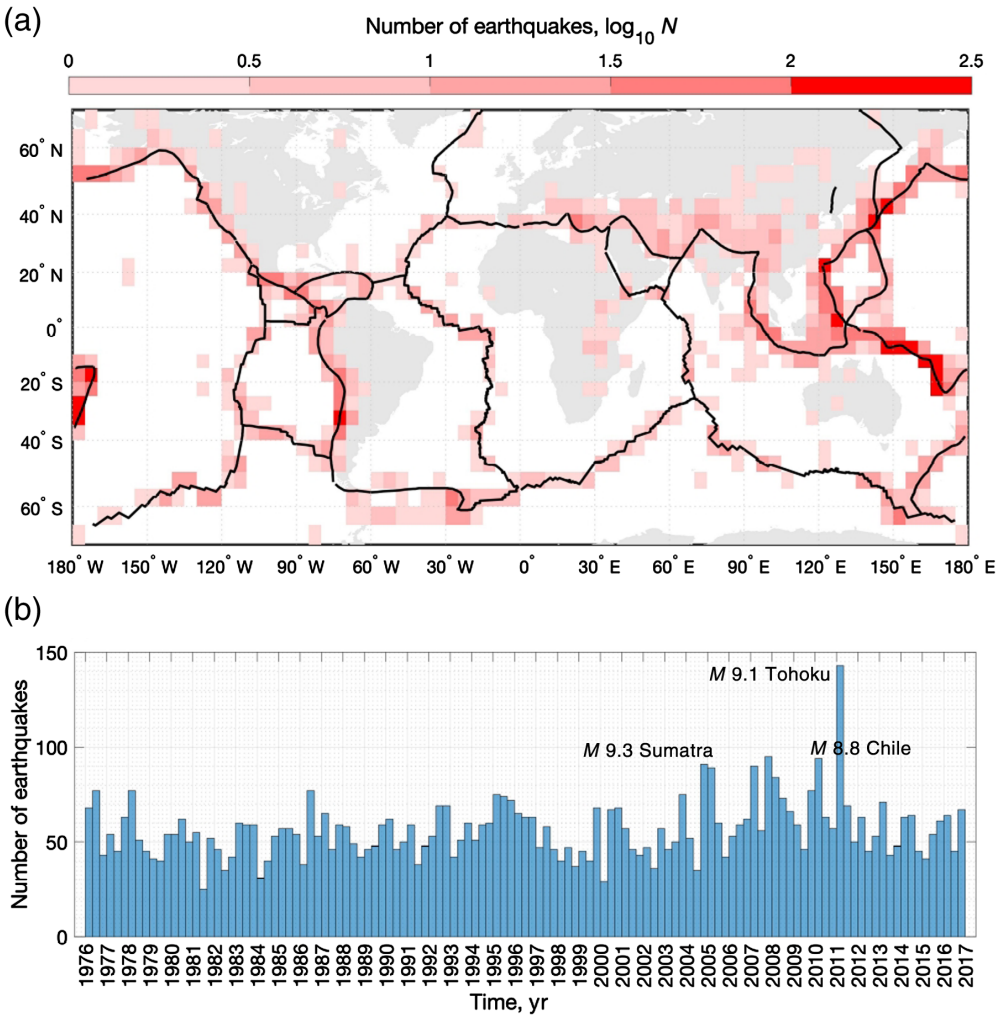

Figure 2. Spatiotemporal clustering of global seismicity based on the International Seismological Centre–Global Earthquake Model (ISC-GEM) v.8 catalog during the period 1976–2017. (a) The number of earthquakes with $M \geq 5.8$ in square spatial cell with latitude side of 5° (color). Black lines show plate boundaries. (b) Event counts in four-month time intervals. Some of the spikes correspond to aftershocks of large earthquakes indicated in the figure; the higher number of events following the M 9.1 Tohoku earthquake relative to the larger M 9.3 Sumatra earthquake illustrates the lack of true universality in earthquake behavior. The color version of this figure is available only in the electronic edition.

space inhomogeneities that mask signals expressed by coupled space–time fluctuations of earthquake rates. These coupled fluctuations include aftershocks, foreshocks, swarms, and multiple other types of clusters that one might want to detect for future examination or removal from the catalog. We discuss some approaches to detecting and removing the coupled space–time inhomogeneities, along with the goals and metrics of catalog declustering.

Clustering of Earthquakes

Basic observations

We begin by illustrating earthquake clustering in southern California, using the high-quality relocated catalog of Hauksson *et al.* (2012, extended to later years) for earthquakes with magnitudes $M \geq 2$ during 1981–2020 (Fig. 1). The catalog lists 89,341 such events within 119.5°–115.5° W and 32.8°–36.5° N, and it features an unprecedented combination of spatial coverage, completeness magnitude, and event location quality. The average absolute horizontal location error for the examined events is 275 m; the completeness magnitude is between 2 and 3, and may slightly vary in time and space (Hauksson *et al.*, 2012). Counting events within 7605 spatiotemporal voxels that have a square spatial projection with a side length equal to 0.25° latitude and duration of 1 yr shows that 38% (2857) of the voxels are empty. The marginal space and time projections of these voxels, with the corresponding event counts, are shown in Figure 1a,b, respectively. The voxel event count has a heavy-tailed distribution (e.g., Kagan and Jackson, 2000) with a highly uneven voxel population. Although the average number of events in the nonempty voxels is 18, the maximal count is 2733, which is 145 times the mean. In other words, about 3% (2733) of the entire catalog is contained within a single voxel, which is only about 0.02% of the examined nonempty space–time volume. This maximal voxel count corresponds to aftershocks of 1992 M 7.3 Landers earthquake.

Similar clustering is seen in other regions and with other magnitude thresholds, so the clustering effect in the southern California catalog is not due to possible catalog artifacts such as completeness issues and event location errors. As a complementary example, we consider 7066 global earthquakes with $M \geq 5.8$ and depth $z < 70$ km during 1976–2017 from the International Seismological Centre–Global Earthquake Model (ISC-GEM) v.8 Global Instrumental Earthquake Catalogue (Storchak *et al.*, 2013, 2015; Di Giacomo *et al.*, 2018). This selection has been reported to be complete in several independent

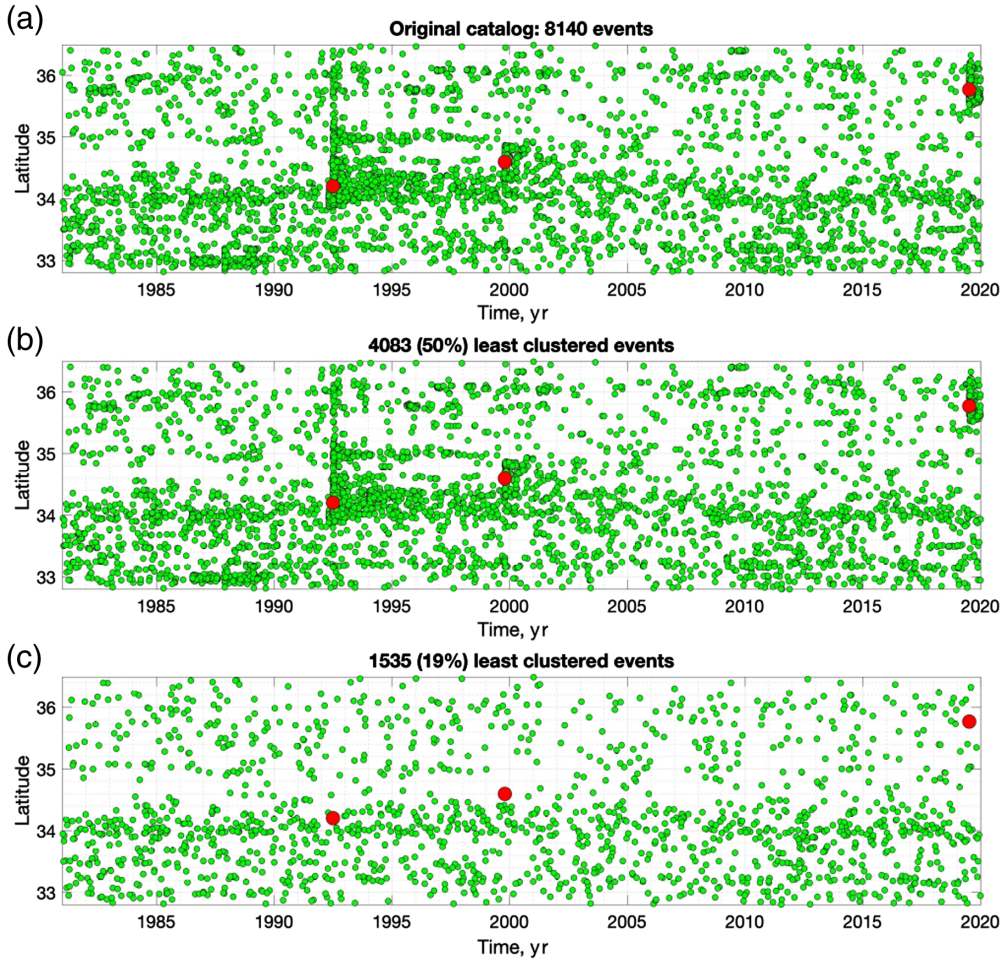

Figure 3. Clustering of seismicity in southern California. Time–latitude projection of earthquakes with magnitude $M \geq 3$ in the catalog of Hauksson *et al.* (2012, extended) during 1981–2020. The largest earthquakes (1992 M 7.3 Landers, 1999 M 7.1 Hector Mine, and 2019 M 7.1 Ridgecrest) are marked by red circles. (a) The full catalog with 8140 events. (b) The 50% (4083) least clustered events. (c) A declustered catalog based on the method of Zaliapin and Ben-Zion (2020) with 19% (1535) least clustered events. The visual similarity of (a,b) shows that 50% of the catalog occurs in dense clusters. The color version of this figure is available only in the electronic edition.

studies (e.g., Michael, 2014; Di Giacomo *et al.*, 2015). The global seismicity occupies a small fraction of the available space, concentrating around the main plate boundaries (Fig. 2a). If we tile the Earth surface by 2592 square spatial cells with latitude size of 5° (Fig. 2a), only 508 (20%) cells contain at least one earthquake and 2084 (80%) cells remain empty. The earthquake distribution is also strongly nonuniform in time (Fig. 2b) mainly because of aftershocks sequences of large earthquakes (e.g., the 2011 M 9.1 Tohoku). The space and time inhomogeneities combine and amplify when one considers the joint space–time distribution of earthquakes. For instance, if we partition the space–time volume of the examined global catalog into 20,736 voxels with a square space projection of 5° latitude and 5 yr duration, 18,866 (90%) voxels remain empty. The number of events in the remaining 1870 (10%) non-empty voxels varies between 1 and 130, with a mean of 3.78. The largest count of 130 corresponds to a voxel around the epicenter of the great 2011 M 9.1 Tohoku earthquake. This single voxel contains 2% of the recorded global seismicity, while representing only 0.005% of the examined space–time.

Figure 3 offers another visual illustration of the strong clustering of earthquakes in southern California. Figure 3a shows the time–latitude projection of all 8140 events with $M \geq 3$ in the catalog. Figure 3b only includes the 50% (4083) least clustered events based on the nearest-neighbor earthquake proximity discussed in Zaliapin and Ben-Zion (2020) and illustrated later. Despite this substantial culling, the panels are barely distinguishable visually. They show the same relative intensity of earthquakes at different latitudes, the same temporal fluctuations, and the same major groups of events. The figure illustrates that at least half of the catalog is in the form of extremely dense clusters not easily discernible by eye. The majority of earthquakes occur within the immediate spatiotemporal vicinity of other events and do not evenly sample the active seismogenic volume.

Figure 3b suggests that a proper declustering of this data set should remove >50% of events, because it still shows visible clusters associated with the 1992 M 7.3 Landers, 1999 M 7.1 Hector Mine, and 2019 M 7.1 Ridgecrest. Figure 3c presents a declustered version of the catalog using the method of Zaliapin and Ben-Zion (2020). The declustered catalog consists of the 19% (1535) least clustered events. The declustering eliminates the prominent clusters illustrated in Figure 3a,b, while preserving the relative rates of events in different regions. This declustering approach is based on the separation of scales in the nearest-neighbor earthquake proximity (Baiesi and Paczuski, 2004; Zaliapin *et al.*, 2008; Zaliapin and Ben-Zion,

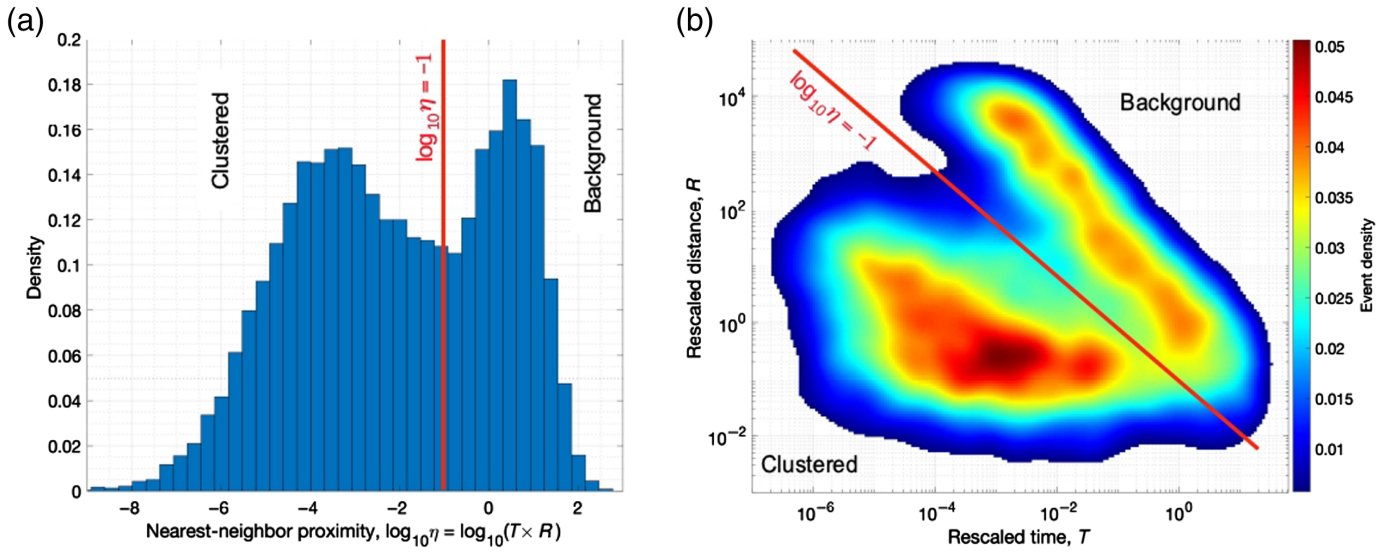

Figure 4. Scale separation in the earthquake nearest-neighbor proximity in southern California, using the catalog of Hauksson *et al.* (2012, extended) with magnitudes $M \geq 3$ during 1981–2020. (a) Bimodal distribution of the nearest-neighbor earthquake proximity η. (b) Bimodal distribution of the time (*x*-axis) and space (*y*-axis) components of the earthquake proximity. Red line ($\log_{10}\eta = -1$) depicts the separation between the cluster (lower proximity) and background (higher proximity) modes in both panels. The two modes are separated by several orders on the proximity scale. This separation of scale facilitates the catalog declustering, but the large number of events around the separation line produces differences between alternative declustering approaches. The color version of this figure is available only in the electronic edition.

2013, 2016). The proximity from any earthquake to an earlier event is defined as a product of the interevent time Δt and surface distance r raised to the fractal dimension d of the events, $\eta = \Delta t r^d$. The distribution of the nearest-neighbor proximity is prominently bimodal in various observed and model catalogs; see Zaliapin and Ben-Zion (2020) for references to specific studies.

Figure 4 shows the bimodal distribution of the nearest-neighbor proximity in the examined catalog of southern California with magnitudes $M \geq 3$ during 1981–2020. Figure 4a and 4b shows the scalar proximity and the joint distribution of its time component $T = \Delta t$ and space component $R = r^d$ that are defined so that $\eta = RT$, respectively. Here, we use $d = 1.6$; although the bimodal nature of the proximity is independent of the parameter selection (Zaliapin and Ben-Zion, 2013). The two modes are separated by several orders on the proximity scale (Fig. 4a), emphasizing the extreme nature of earthquake clustering. The two modes are also well separated in space–time (Fig. 4b). The cluster mode (lower proximity values) is mainly composed of aftershock sequences and swarms, and is primarily responsible for the space–time clustering discussed and quantified in this work. The declustering illustrated in Figure 3c involves stochastic thinning based on the proximity values; this helps avoiding a sharp cut along the model separation line, which might result in artificial inhomogeneities of the declustered catalog (Zaliapin and Ben-Zion, 2020).

An informative way to look at earthquake clustering is to estimate how many events are offspring of background events, and hence may be viewed statistically as being triggered. In the absence of clustering, each event belongs to the background activity and does not produce offspring. In contrast, a high clustering implies that a large proportion of earthquakes are offspring to a small number of parent events. We estimate the offspring relations using the nearest-neighbor approach; informally, an event is considered an offspring if its nearest neighbor proximity η to an earlier event (parent) belongs to the cluster mode of the bimodal diagram of Figure 4.

Figure 5a shows the proportion of offspring events (*y* axis) versus the proportion of parent events (*x* axis) for earthquakes with $M \geq 2$ in the catalog of Hauksson *et al.* (2012, extended) for southern California during 1981–2020. The degree of estimated offspring productivity (triggering) is striking: the single 1992 M 7.3 Landers earthquake has 15,389 (17%) offspring, and over 50% of the events in the catalog are estimated offspring to mere 77 earthquakes with $M \geq 5$. Figure 5b illustrates the offspring analysis for several other regions examined in this study; they all show a high offspring productivity (measured by the deviation from the diagonal).

The results in Figures 1–5 suggest that the majority of events in the observed earthquake catalogs belong to clusters that occupy a small highly active part of the examined space–time volume. This active part reflects primarily the particular set of large events that occurred during the data acquisition period and generated numerous aftershocks. This part might be not representative of the long-term processes in the region. For instance, large sections of the San Andreas and other major

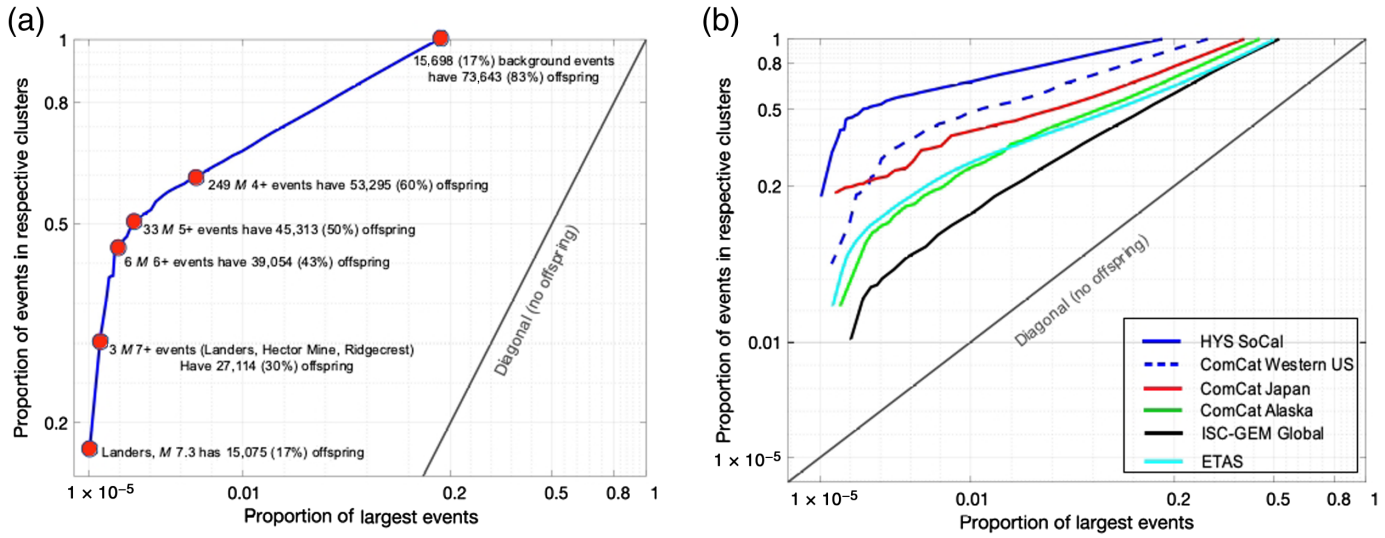

Figure 5. Triggering diagram for earthquakes in (a) southern California and (b) other regions. Proportion of offspring (*y* axis) produced by a given proportion of the largest earthquakes (*x* axis). The offspring relations are identified by the method of Zaliapin and Ben-Zion (2020). The diagonal line corresponds to the absence of triggering (all events belong to the background). The deviation of the observed line from the diagonal signifies a large fraction of offspring events. The axes are scaled with a power of 0.25 to zoom-in the left part of the diagram, highlighting that a very small number of largest events triggers a significant fraction of the catalog. (a) Earthquakes with magnitude $M \geq 2$ in the Hauksson *et al.* (2012, extended) catalog during 1981–2020. (b) All catalogs examined in the study; see Table 1 for catalog description. ComCat, comprehensive catalog. The color version of this figure is available only in the electronic edition.

faults in southern California have been relatively inactive during the data acquisition period 1981–2020 in the Hauksson *et al.* (2012, extended) catalog. Similarly, the two $M \geq 9$ earthquakes in the examined ISC-GEM catalog (2004 M 9.3 Sumatra–Andaman and 2011 M 9.1 Tohoku) occurred in Asia and do not fully represent regions prone to M 9-class earthquakes (e.g., the Pacific Rim). We show below that earthquake clustering goes beyond the existence of relatively small active space–time domains (nonempty voxels in the analysis of Figs. 1 and 2) and extreme offspring productivity of the largest events (Figs. 3 and 5). The nonuniform heavy-tailed event distribution is seen generically within seismically active space–time volumes, biasing statistical analyses of seismicity at a variety of scales and with different event- and region-selection criteria.

To reduce the bias caused by space–time clustering and study more representative long-term processes, it is important to sample the entire seismogenic volume more evenly. This is the basic goal of catalog declustering. To inform declustering efforts, we introduce a formal framework for assessing the degree of earthquake clustering and show that strong clustering is a common robust feature of multiple seismically active regions. We illustrate the analysis using the observed earthquake catalogs of southern California, western United States (WUS), central and eastern United States (CEUS), Alaska, Japan, global seismicity, and a synthetic catalog of the epidemic-type aftershock sequence (ETAS) model.

Quantifying clustering: ROC diagram of earthquake space–time distribution

To systematically quantify the inhomogeneity of the space–time distribution of seismicity, we use the receiver operating characteristic (ROC) diagrams, following Ben-Zion and Zaliapin (2020). Specifically, we partition the examined space–time volume into voxels, count events in the voxels, and construct a diagram (Fig. 6a) that shows the proportion of events in the most populated voxels (*y* axis) versus the proportion of such voxels (*x* axis). Section A of the supplemental material formally defines the diagram. Considering only nonempty voxels ensures that the analysis is not affected by selection of the boundaries of the examined region, which can have a strong effect on the number of empty voxels. We note also that using only nonempty voxels decrease the estimated degree of clustering. The sorting of counts implies that the diagram always stays above the diagonal and connects the origin to the upper-right corner (1,1).

The diagonal line corresponds to a constant count within nonempty voxels. It may be useful to think of a constant count as the expected value of a model that assigns an identically distributed event counts to all examined voxels, for example, uniform distribution of events among the voxels. Convexity of the diagram (deviation from the diagonal) reflects nonuniformity in the event distribution; a large number of events occur within a small number of voxels. Observe that the ROC analysis only focuses on relative rates of events in different voxels and not on the absolute values of the rates. We quantify the nonuniformity of the ROC diagram by the Gini coefficient G defined as twice

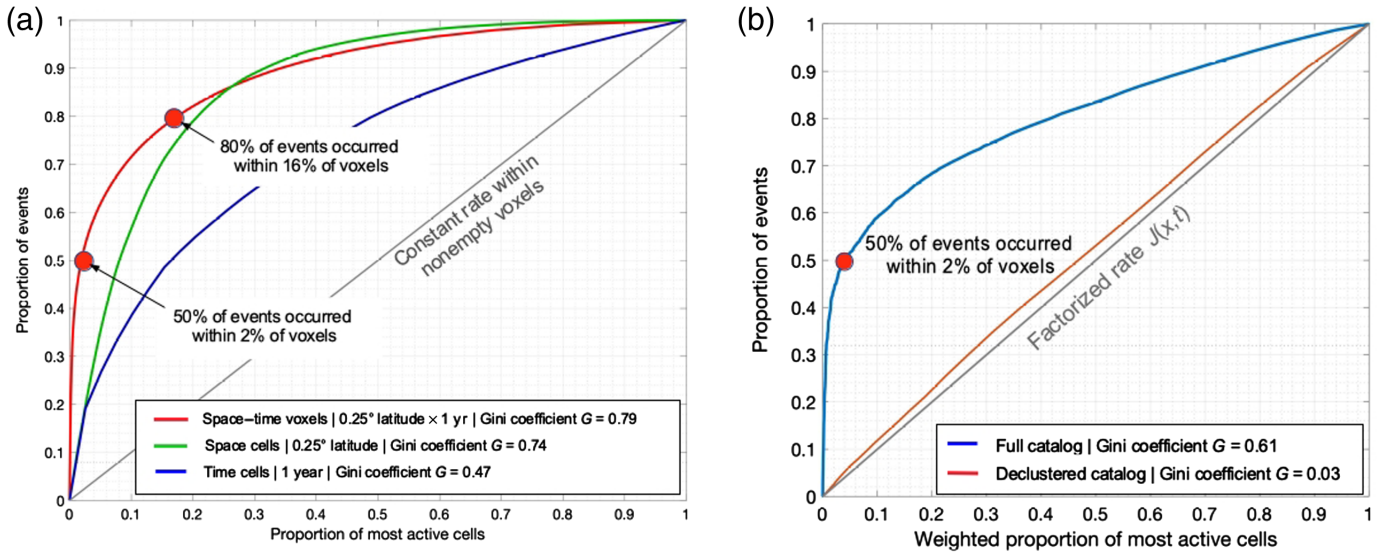

Figure 6. Quantifying clustering of earthquakes in southern California with the receiver operating characteristic (ROC) diagram. The analysis uses the catalog of Hauksson *et al.* (2012, extended) during 1981–2020 with magnitude $M \geq 2$, and space–time voxels with square space projection of latitude size 0.25° and 1 yr duration. (a) Proportion of earthquakes (*y* axis) that occurred within a given fraction (*x* axis) of the most active voxels. The diagonal line corresponds to a constant rate of events in the nonempty voxels. The results for the joint space–time partition are shown by the red line; results for the marginal space and time partitions are shown by green and blue lines, respectively. (b) The proportion (*y* axis) of earthquakes that occurred within a given weighted fraction (*x* axis) of voxels. The weight of a voxel is proportional to the number of background events that occurred within the space projection of the voxel during the entire examined time interval. The diagonal line corresponds to the factorized rate $J(x,t)$ of events with marginal space and time distribution taken from the estimated background. The deviation of the observed line (blue) from the diagonal signifies temporal fluctuations of event rate within local areas (coupled space–time inhomogeneities). The red line corresponds to a declustered catalog (background events). The background events are identified using the method of Zaliapin and Ben-Zion (2020). The color version of this figure is available only in the electronic edition.

the area between the diagram and the diagonal line. All realistic values of G are within the interval (0,1), where 0 corresponds to constant counts and 1 to an extreme concentration of all events within a single voxel. Tracking the temporal evolution of G provides a way of analyzing evolving localization of seismicity, as was done in Ben-Zion and Zaliapin (2020). Here, we focus on a cumulative value of G calculated for an entire examined space–time volume.

To develop intuition about the G scale, Figure 7 shows three 1D synthetic examples of nonzero event counts with different degrees of nonuniformity (Fig. 7a–c) and their ROC diagrams with respective G values (Fig. 7d). All examples correspond to 50 cells with comparable average event counts. Figure 7a shows the most clustered sequence. The event counts substantially deviate from their mean value, varying between 1 and about 800; this corresponds to $G = 0.76$. Figure 7b shows an intermediate clustering with event counts between 1 and roughly 200; here $G = 0.49$. Figure 7c shows the least clustered sequence in which all counts are close to the mean of 50, and G is about 0.1.

The ROC diagram for the space–time partition of the southern California seismicity shown in Figure 6a (red) has $G = 0.79$. In particular, we observe again that 50% (44,638) of the events are contained within only 2% (86) of nonempty voxels, and 80% (71,464) of the events are contained within only 16% (478) of nonempty voxels. The corresponding diagrams for the marginal spatial (green) and temporal (blue) partitions of events illustrated in Figure 1a and 1b have G values of 0.74 and 0.47, respectively. The spatial clustering is evidently stronger than the temporal clustering, and the joint space–time partition is more clustered than each of its marginals.

Focusing on coupled space–time clustering

The high degree of clustering in our analysis of southern California seismicity (Fig. 6) is strongly affected by the concentration of seismicity around the main faults (Fig. 1a) and strong decay of earthquake rates with distance from the fault cores. Indeed, the space (green) and space–time (red) clustering diagrams in Figure 6a are similar to each other, and the respective G values of 0.74 and 0.79 are close as well. This suggests that the marginal space inhomogeneity of earthquake distribution (related to the active fault network) contributes significantly to the overall earthquake clustering. In other words, the space–time (red) curve in Figure 6a would be convex, and the respective clustering would be high, even for a stationary rate of seismicity, simply because some regions are more active (during the data acquisition period) than the others. The clustering can be similarly affected by the marginal time inhomogeneities. Such marginal inhomogeneities may represent the actual long-term

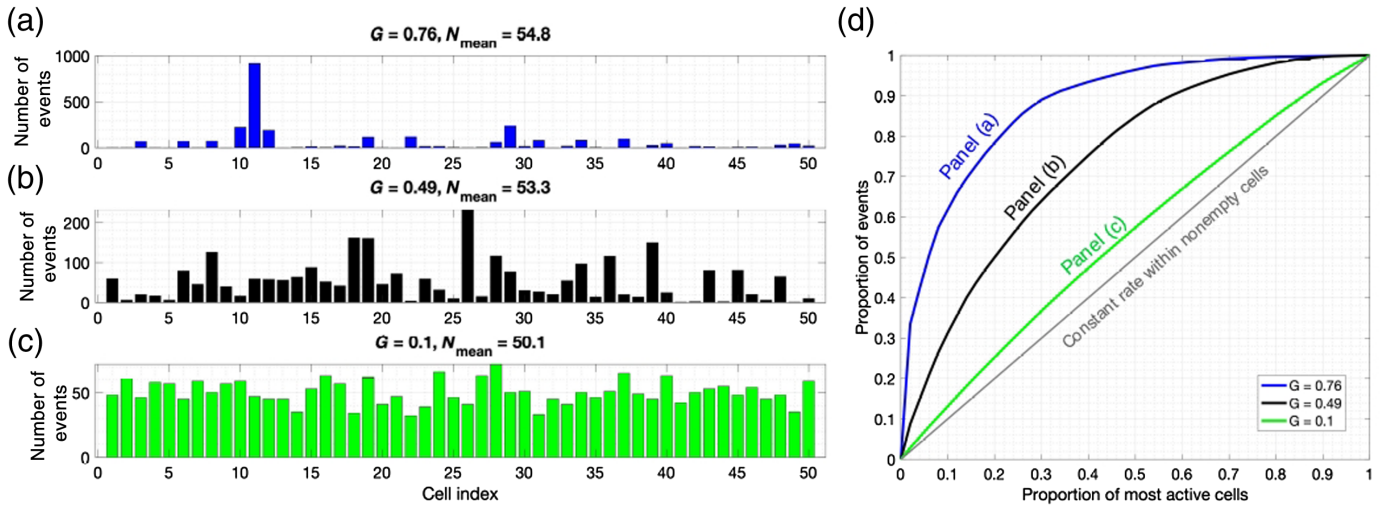

Figure 7. Synthetic examples of ROC clustering analysis. Three synthetic sequences of nonzero cell counts with 50 distinct values and average cell count of about 50 have Gini coefficients of (a) G = 0.76, (b) G = 0.49, and (c) G = 0.1. Their ROC diagrams are shown in (d). The color version of this figure is available only in the electronic edition.

dynamics of seismicity. We would like to eliminate the effects of marginal space and time inhomogeneities on clustering, and only quantify the coupled space–time variations.

The ROC framework is well suited for achieving this goal. This is illustrated in Figure 6b where the x axis is scaled in such a way that the product $J(x,t) = S(x)T(t)$ of the marginal space $S(x)$ and marginal time $T(t)$ rates of the estimated background seismicity corresponds to the diagonal. Formally, the x axis in Figure 6b shows the proportion of the factorized rate $J(x,t)$ within the most active cells of the examined process, and the y axis shows the respective proportion of events in the examined process. Section A of the supplemental material formally defines this scaled version of the diagram and illustrates (Fig. S1) a calculation of the factorized rate. In this analysis, the marginal space and time inhomogeneities are reflected by $J(x,t)$ and hence are mapped onto the diagonal. Only coupled space–time irregularities—short-term temporal fluctuations in local areas—cause deviation from the diagonal. The overall degree of the coupled space–time clustering is measured by the Gini coefficient G of this scaled ROC diagram.

The blue curve in Figure 6b corresponds to the full catalog and the red curve to a declustered version based on the nearest neighbor methodology of Zaliapin and Ben-Zion (2020). We also use this declustering method for estimating the background activity used in calculating the factorized rate $J(x,t)$. Figure 6b demonstrates that the overwhelming majority of events in the full catalog occur within a very small fraction of the seismically active volume, even after controlling for the marginal space and time irregularities. For example, 50% of the events occurs within 2% of weighted voxels (red circle). This reflects coupled spatiotemporal clustering mainly caused by aftershock sequences and swarms, and not the concentration of events along the fault network. The declustered catalog (red line) lacks this space–time coupling, and its ROC diagram closely follows the factorized intensity $J(x,t)$.

Figures S2–S4 and Table S1 illustrate high stability of the ROC-based clustering analysis with respect to the following choices: (1) lowest examined magnitude, (2) space and time sizes of partition voxels, and (3) the number of background events in a declustered catalog. In particular, our analysis of southern California seismicity with magnitude $M \geq 2$ indicates that the clustering Gini coefficient G varies roughly within ±0.1 unit when changing the lowest magnitude within 2 units (between 2 and 4), the number of examined events within 2 orders (between 89,000 and 800), the duration of time discretization within 2 orders (between one month and 10 yr), the lengths of space cells within 1 order (between 3 and 100 km), and the number of estimated background events between 10% and 25% of the full catalog. In the examined cases, the G coefficient was found to be representative if the average number of events in nonempty voxels is above 5 and total number of voxels is above 300.

Clustering in other regions and ETAS model

To further illustrate clustering properties, we analyze several other seismically active regions and synthetic seismicity of the ETAS model. The catalogs are described, and the results are summarized in Table 1. Specifically, we use the U.S. Geological Survey (USGS) comprehensive catalog to examine seismicity of the WUS using events with $M \geq 3$ (Table 1, row 2); CEUS east of Kansas and Nebraska (to exclude induced seismicity that dominates some areas) using events with $M \geq 2.5$ (row 3); Japan using events with $M \geq 4$ and depth less than 70 km (row 4); and Alaska using events with $M \geq 4$ and depth less than 70 km (row 5). We use the ISC-GEM v.8 catalog to examine the global seismicity (row 6). Finally, we

TABLE 1
Summary of Clustering Analyses in Southern California, Western United States (WUS), Central and Eastern United States (CEUS), Alaska, Japan, Global International Seismological Centre–Global Earthquake Model (ISC-GEM) Catalog, and Epidemic-Type Aftershock Sequence (ETAS) Model

Number	Catalog	Space Range	Time Range	Magnitude Range	Number of Events	α_0*	Number of Background Events†	Clustering with Respect to Constant Rate‡, Mean G (95% CI)	Clustering with Respect to Factorized Rate $J(x,t)$‡, Mean G (95% CI)	Background Clustering with Respect to Factorized Rate $J(x,t)$‡, Mean G (95% CI)
1	HYS SoCal	119.5°–115.5°W; 32.8°–36.5°N	1981–2020	2.0–7.3	89,341 (100%)	0	15,914 ± 110 (17.8% ± 0.1%)	**0.77** (0.7, 0.82)	**0.55** (0.35, 0.63)	**0.031** (0, 0.06)
2	ComCat WUS	126°–110° W; 30°–50° N	1981–2021	3.0–7.3	30,483 (100%)	0	8,494 ± 72 (27.9% ± 0.24%)	**0.74** (0.59, 0.82)	**0.38** (0.2, 0.48)	**0.029** (0, 0.07)
3	ComCat CEUS	95°–60° W; 30°–50° N	1981–2021	2.5–5.9	2,591 (100%)	0	1,172 ± 27 (45.2% ± 1.03%)	**0.63** (0.51, 0.71)	**0.17** (0.07, 0.28)	**0.029** (0, 0.06)
4	ComCat Japan	138°–146° W; 32°–44° N	1974–2021	4.0–9.1	17,823 (100%)	0	5,885 ± 59 (33.0% ± 0.33%)	**0.67** (0.57, 0.72)	**0.39** (0.07, 0.51)	**0.044** (0, 0.09)
5	ComCat Alaska	180°–120° E; 45°–75° N	1973–2020	4.0–8.0	15,008 (100%)	0	6,682 ± 56 (44.5% ± 0.37%)	**0.71** (0.6, 0.81)	**0.18** (0.06, 0.29)	**0.002** (–0.02, 0.02)
6	ISC-GEM	World	1976–2017	5.8–9.3	7,066 (100%)	0	3,680 ± 41 (52.1% ± 0.58%)	**0.64** (0.57, 0.72)	**0.11** (0.07, 0.16)	**0.006** (0, 0.03)
7	ETAS	600 × 600 km	20.9 years	2.5–7.3	26,986 (100%)	0	7,130 ± 73 (26.4% ± 0.27%)	**0.66** (0.58, 0.71)	**0.05** (–0.09, 0.32)	**0.002** (–0.02, 0.03)

ComCat, comprehensive catalog.
*Cluster threshold that controls the number of background events (Zaliapin and Ben-Zion, 2020).
†Mean and 95% confidence interval (CI) according to 10^4 realizations of stochastic declustering. The CI is estimated as ±1.96 sample standard deviation.
‡Estimation is done for the space–time partitions with the average of at least five events per nonempty voxel and at least 300 voxels total. The CI limits are the 0.025 and 0.975 sample quantiles.

examine a version of the ETAS model (row 7) with spatial parameters fitted for southern California by Gu *et al.* (2013). We keep the same clustering analyses parameters as those used for the southern California catalog, other than increasing the linear dimension of space cells to 1000 km for all catalogs except ETAS, to reflect their larger spatial extent. The southern California results that we discussed and illustrated in earlier sections are listed in row 1 of Table 1.

All examined catalogs show similar general clustering patterns. The overall degree of clustering, measured by the clustering coefficient G of a full catalog with respect to constant rate (column 9), has the highest value, which is above 0.6 in all examined cases. The variability of this clustering value with respect to the space–time resolution is mild, roughly within ±0.1 unit. This mainly reflects complex geometry of the fault networks, concentration of earthquakes around the faults, and decay of earthquake rates off the faults. The coupled space–time clustering independent of space and time marginal fluctuations, measured by clustering of a full catalog with respect to the factorized rate $J(x,t)$ (column 10), has smaller, and still well confined, values of G. The WUS and Japan catalogs have the highest coupled space–time clustering, with G = 0.38 and 0.36, respectively. The CEUS and Alaska show lower coupled space–time clustering, with G = 0.17 and 0.18, respectively. The global ISC-GEM catalog has the lowest clustering among the examined natural seismicity cases, with G = 0.11. In the observed seismicity catalogs, G has a negative relation with the estimated proportion of background events, which is expected according to its definition. The coupled space–time clustering of declustered catalog, measured by clustering of background events with respect to the factorized rate (column 11), is always below 0.05.

The ETAS model with parameters fitted for southern California by Gu *et al.* (2013) has a substantially lower degree of clustering G (Table 1, row 7) than that of the observed southern California seismicity, despite comparable space, time, and magnitude ranges of the two catalogs. The clustering measure G of the full ETAS catalog with respect to the constant rate (column 9) is G = 0.66. This value and the respective 95% confidence interval (CI) of (0.58, 0.71) are below the value G = 0.77 that is observed for the real catalog of this region (Table 1, row 1). An even bigger difference with respect to the observed seismicity is seen in clustering of the full ETAS catalog with respect to the factorized rate $J(x,t)$ (column 10): The average Gini coefficient in the model is merely G = 0.05 with the CI of (−0.09, 0.32), which is comparable to the G values in the declustered observed catalogs. This indicates that the examined ETAS catalog has no substantial space–time coupling beyond that dictated by inhomogeneous background distribution. This is related to the following three features of the ETAS model. (1) The model aftershock sequences are very short compared with the observed aftershock sequences. Accordingly, although the degree of clustering increases (up to G = 0.3) for short time discretizations that are comparable to the typical aftershock duration, it remains low for time discretizations that are longer that the typical aftershock duration. As a result, the average clustering value reported in the Table 1 is low. (2) The largest earthquakes occur within the most active space regions, which is often not the case in actual observations. (3) The rate of clustered events is proportional to the overall region activity, because each event of a given magnitude has the same offspring productivity independently of its location or occurrence time. This is not the case in natural data, in which different regions may have different productivity rates, and clustering may change with time (especially for swarms). The last two features imply that the clustered seismicity in the examined version of ETAS provides a reasonable sampling of the model background event distribution (i.e., areas with higher or lower rates of background events would have higher or lower rates of clustered events, respectively), although the rates of clustered and background events are not linearly related. This is different from observed seismicity, where high clustering rates may correspond to low background rates (e.g., the aftershock sequence of 1992 M 7.3 Landers earthquake in southern California), and low clustering rates may correspond to high background rates (e.g., the Geysers geothermal area). This explains why the degree of space–time factorization is much higher, and the clustering measure G is much lower, in the ETAS model compared to that in the examined observed catalogs. The results indicate that properties of observed seismicity are significantly less homogeneous than those in the examined ETAS model with parameters fitted regionally. The ETAS parameters can be fitted adaptively to different regions or even to individual aftershock sequences (e.g., Enescu *et al.*, 2009), which would likely improve the correspondence between the clustering properties of the ETAS model and observations.

Declustering Earthquake Catalogs

The high spatiotemporal clustering of earthquakes illustrated in Figures 1–6 and Table 1 implies that the statistical properties of a full catalog can be dominated by a miniscule space–time volume highlighted by aftershocks of the largest observed events. Our results suggest that clustering (triggering) might be responsible for the overwhelming majority of events in a catalog (Fig. 5). The actual clustering might be even higher than those estimated here, because some events may be triggered by earthquakes outside the examined space–time region (van der Elst, 2017). A full catalog strongly amplifies short-term triggering relative to the long-term interseismic background processes. Catalog declustering is aimed at removing this bias and facilitating analyses of additional, subtler, features of seismicity.

In addition to addressing why it might be essential to decluster earthquake catalogs, it is important to consider carefully how to decluster. At present, there is no physical criterion that can separate independent (background) earthquakes from

dependent (clustered, triggered) ones. More elementally, because the dynamics of seismicity is an unsolved problem (e.g., Ben-Zion, 2008), we do not know to what extent natural processes operate in these terms (background, clustered, mainshock, foreshock, and so forth). Therefore, the problem of earthquake declustering has neither a definite physical nor mathematical formulation, and the desired form of a declustered catalog may depend on the application at hand. In some problems, such as stress inversions of focal mechanisms (Michael, 1987; Vavryčuk, 2014; Martínez-Garzón *et al.*, 2016), it is useful to retain the largest number of background events likely to be produced by the remote tectonic loading, even if the resulting catalog remains nonstationary. In other problems, such as evaluating long-term seismic hazard (Petersen *et al.*, 2018; Llenos and Michael, 2020), it may be desired to obtain a quasi-stationary background activity, even if this means removing additional events. There are numerous sources of nonstationarities in modern high-quality catalogs (e.g., Hauksson *et al.*, 2012; Ross *et al.*, 2019), including nontectonic triggering (e.g., Bettinelli *et al.*, 2008; Johnson *et al.*, 2019; Hsu *et al.*, 2021), nonstationary postseismic relaxation below the seismogenic crust (e.g., Ben-Zion *et al.*, 1993; Pollitz *et al.*, 2014), and various catalog uncertainties (e.g., Kagan, 2003; Hauksson *et al.*, 2012; Zaliapin and Ben-Zion, 2015). Accordingly, a stationary declustered catalog—a renowned Poisson process of background events discussed in the classic works of Gardner and Knopoff (1974) and Reasenberg (1985)—is not necessarily an appropriate target. More generally, it seems that any hard and fast statistical criterion of a declustered catalog can be easily falsified with modern tools, yet often in a noninformative way (Luen and Stark, 2012). Because there is no unique physical theory of earthquake clustering, there is no unique "right solution" to the declustering problem. The statistical and physical criteria of a desirable declustering for a given problem should meet in the middle. Declustering should be viewed as an interactive process, allowing an expert user to resolve a trade-off between the number of background events and their emerging properties (e.g., time homogeneity, coupled space–time clustering, and so forth). Examining a range of possible backgrounds and the implied results for a problem at hand may be more informative than a judicious selection of a single "correct" declustering. Quoting Utsu (1970, 132 pp.), "… a definition of aftershocks uniformly applicable to all kinds of aftershock problems is difficult to establish, and a suitable working definition must be formulated according to the character of the problem and the data employed." Increasingly comprehensive data sets, statistical techniques, and computing power provides new opportunities and challenges for making suitable working definitions for different purposes.

Declustering significantly modifies the catalog and may alter its key statistical attributes, such as *b*-value (relative proportion of large and small events), *a*-value (earthquake annual rate), fractal dimension of hypocenters, relative rates of events in different regions, and so forth (e.g., Knopoff, 2000; van Stiphout *et al.*, 2011; Llenos and Michael, 2020; Mizrahi *et al.*, 2021; Taroni and Akinci, 2021). Different types of declustering affect various attributes to different extents. For example, declustering may start with identifying clusters and then selecting a single event from each cluster as background (and remove all other events as clustered). The two most popular choices are the first event or the largest event. Selecting the first event from each cluster might not significantly affect the *b*-value (e.g., Llenos and Michael, 2020), but in this case the largest event in the catalog may not belong to the background. Selecting the largest event from each cluster retains the largest events (mainshocks) as background, but this will necessarily deflate the *b*-value increasing the relative proportion of large events (Mizrahi *et al.*, 2021). As mentioned, the choice of declustering method and its implementation (e.g., parameter selection) should be made by the user. An informed decision would consider various aspects of the examined catalog—the maximal magnitude, the range of magnitudes, level of completeness, inhomogeneity of spatial distribution, degree of clustering, regional cluster style, as well as how the declustered catalog will be used. The ROC-based clustering framework presented here might be a useful tool in assessing the degree of marginal and coupled space–time clustering and guiding a user in quantifying an appropriate degree of declustering suitable for the problem at hand. For example, the declustering technique of Zaliapin and Ben-Zion (2020), which we use in this work, involves a threshold parameter α_0 that controls the number of estimated background events in a declustered catalog. Depending on the value of α_0, the declustered catalog will have a larger or smaller number of events, although the relative spatial earthquake background rates (that reflect the existence of high- and low-activity regions) is preserved. A possible criterion for selecting a proper threshold, and hence the number of background events, could involve estimating the clustering coefficient $G = G(\alpha_0)$ of a declustered catalog for different values of α_0 and selecting the threshold that corresponds to the maximal number of background events with G below a predefined value G_0. Table S1 illustrates the variability of background level as a function of the threshold α_0 and demonstrates stability of our clustering results with respect to this parameter.

There are several approaches (and respective algorithms) for declustering seismicity, each with its pros and cons. We refer to van Stiphout *et al.* (2012) for a technical review of the methods up to that time. The classical window technique initiated by Knopoff (1964) and Gardner and Knopoff (1974) and its ramifications (e.g., Uhrhammer, 1986; Rosson *et al.*, 2019) are intuitive and simple to implement; this approach is traditionally used in the USGS National Seismic Hazard Map (Petersen *et al.*, 2018). However, there is an increasing awareness that window techniques can be incommensurable

with the quality and detail of modern catalogs (e.g., Teng and Baker, 2019; Peresan and Gentili, 2020). The most obvious drawback is the appearance of holes (regions with no activity) around large earthquakes, which may be inconvenient for further analyses. A more elaborate technique of Reasenberg (1985) connects events in clusters according to adaptive space–time interaction zones and provided good performance in California (for which it has been originally developed) and other regions. This technique has several parameters that might be region and catalog dependent.

Approaches based on the ETAS model (e.g., Zhuang *et al.*, 2002; Console *et al.*, 2010; Llenos and Michael, 2020) have mathematical appeal and are effective for treating major aftershock sequences (e.g., Woessner *et al.*, 2011; Field *et al.*, 2017; Shcherbakov, 2020), but they can have many parameters and may be computationally demanding (e.g., Veen and Schoenberg, 2008). The ETAS model assumes a rigidly parameterized conditional intensity of earthquake clusters, so its appropriateness depends on how well this assumption is met by the examined data and how well one can estimate the multiple model parameters (Ogata, 1999; Wang, Schoenberg, and Jackson, 2010; Schoenberg, 2013; Seif *et al.*, 2017). A more flexible approach of Marsan and Lengline (2008) offers a possibility to work with an arbitrary (but fixed for the entire catalog) cluster model. Declustering is reduced here to estimating the triggering kernel, which is done by recursive approximation. The declustering method of Zaliapin and Ben-Zion (2020) used in the present work is more exploratory and parsimonious in spirit. It uses a nonparametric definition of a cluster, which is quantified using the nearest-neighbor earthquake proximity (Baiesi and Paczuski, 2004; Zaliapin and Ben-Zion, 2013, 2016). The method is highly robust with respect to its parameters and various catalog imperfections, and allows users to select different degree of declustering (different number of background events) while preserving the relative spatial rates of events in different regions. The nonparametric nature of this technique makes it possible for different forms of clustering to coexist in different parts of the catalog. Notwithstanding its nonparametric nature, the technique can closely reconstruct a time-stationary space-inhomogeneous Poisson background of the parametric ETAS model (Zaliapin and Ben-Zion, 2020). This flexibility comes at a price of not having an optimization procedure, as is common in nonparametric methods (e.g., Wasserman, 2006).

Alternative declustering techniques can produce comparable results in selected problems and data sets. For example, the nearest-neighbor declustering of Zaliapin and Ben-Zion (2013, 2020) produces results comparable with that of (1) the Regionally Optimized Background Earthquake Rates from ETAS method in application to probabilistic seismic hazard assessment of induced seismicity of Oklahoma and Kansas and tectonic seismicity of the San Francisco Bay area (Llenos and Michael, 2020), (2) the Reasenberg (1985) declustering and hazard analysis of Oklahoma and Kansas (Teng and Baker, 2019), (3) ETAS stochastic declustering on Zhuang *et al.* (2002) in seismicity of northeastern Italy and western Slovenia (Varini *et al.*, 2020), and some other methods and regions (e.g., Peresan and Gentili, 2020; Mizrahi *et al.*, 2021). At the same time, other problems and/or data sets may be more sensitive to specific aspects of the used declustering method (e.g., van Stiphout *et al.*, 2011; Mizrahi *et al.*, 2021).

A useful perspective on declustering is provided by the existence of two characteristic space–time scales in earthquake dynamics that was illustrated in the bimodal distributions in Figure 4. Multiple declustering algorithms successfully and consistently eliminate the bulk of the cluster mode (even if this mode is not explicitly defined or used in the declustering procedure) and keep the bulk of the background mode, which is facilitated by the previously mentioned scale separation. Some declustering methods still leave a collection of events with quite complex space–time patterns and remaining clustering. The main differences among alternative declustering approaches concern treating the neighborhood of the red line in Figure 4 that separates the modes. Notwithstanding the overall scale separation, this neighborhood includes a substantial proportion of the catalog, so the results of different procedures may differ significantly.

Discussion

This article illustrates the general existence of strong coupled space–time clustering of natural earthquakes that remains after accounting for the marginal space and time inhomogeneities of observed catalogs. The ROC-based Gini coefficient G provides an efficient and stable tool for quantifying the degree of coupled space–time clustering. The degree of earthquake clustering is substantially stronger than what might be suggested by visual inspections (Fig. 3) and modeling based on the ETAS framework with parameters based on a regional fitting (Table 1). Studies aiming at uncovering additional features of seismicity beyond the strong clustering dominated by aftershocks of the largest events or expected long-term properties can benefit from catalog declustering prior to the analyses.

The ROC diagram with the factorized earthquake intensity $J(x,t)$ (see the Focusing on Coupled Space–Time Clustering section) provides a convenient assessment of the coupled space–time clustering in a catalog (Fig. 6b). Large values (close to 1) of G indicate that a large proportion of events is concentrated in a small fraction of the examined space–time volume, and this concentration is not explained by the active fault networks (the entire ROC diagram gives more complete information). This implies that some statistical analyses might be biased, having an amplified focus on the concentration regions in the examined catalogs and not reflecting general long-term properties of seismicity in the regions. Previous applications of the ROC diagram to problems of seismicity used the version of the Quantifying Clustering: ROC Diagram of Earthquake Space–Time Distribution section and Figure 6a (Zeng *et al.*, 2018; Ben-Zion and Zaliapin, 2020). The new alternative version

demonstrated in Figure 6b and section A of the supplemental material is more informative about coupled space–time clustering properties. It distinguishes between persistent spatial fluctuations of rate that take place during the entire examined time interval (factorized case) and fluctuations that are only seen during short time periods (nonfactorized case). Similarly, it distinguishes between persistent temporal fluctuations that affect the entire examined space (factorized case) and only local areas (nonfactorized case).

The ROC approach may also facilitate assessing the quality of declustering; a properly declustered catalog would correspond to an almost-diagonal ROC diagram and a small clustering value G. Notably, this approach is not aimed at obtaining a stationary declustered catalog, which might be an improper target (at least for some studies). Instead, it defines a target of declustering as a catalog with a fully factorized event rate. A declustered catalog that passes the proposed factorization test may include temporal variations of event rates caused by long-term processes not related to event–event triggering (e.g., regional changes in the background intensity due to viscoelastic deformation in the lower crust or anthropogenic activities). The proposed clustering measure G (and other possible metrics of the ROC diagram) complement the currently used measures of declustering quality (Luen and Stark, 2012; Zaliapin and Ben-Zion, 2020). More generally, we propose that the quality of declustering should be assessed not via the properties of the final product (e.g., stationary sequence of events) but via the degree to which the catalog inhomogeneities (and related biases) have been removed.

As is mentioned in the Introduction, a catalog may include earthquakes that are triggered by events outside of the examined space–time domain (Wang, Jackson, and Zhuang, 2010; van der Elst, 2017). Such events may form acute clusters that disturb the space–time factorization of the examined catalog (e.g., aftershocks of a large event just outside of the examined region), or they can be evenly distributed over the examined domain (e.g., remote aftershocks of all events outside the examined region, as discussed by van der Elst, 2017) and closely fit a factorized rate approximation. In the former case (nonfactorized rate), the clustering measure G would readily detect the cluster, although its parent event is not available for analysis. The declustering method of Zaliapin and Ben-Zion (2020) used here can efficiently remove such clusters. This is possible because the relative proximities of neighboring events (which is the main information used for declustering) substantially varies within an aftershock sequence even if the mainshock is not observed. Some alternative declustering techniques can also easily detect such clusters. In the latter case (factorized rate), we note that evenly distributed remote aftershocks that dominate current seismicity (van der Elst, 2017) were only shown so far in the context of the ETAS model. They can also be produced by other models that attribute current activity to distant parents. However, the same events may also be explained differently (e.g., as background) using models

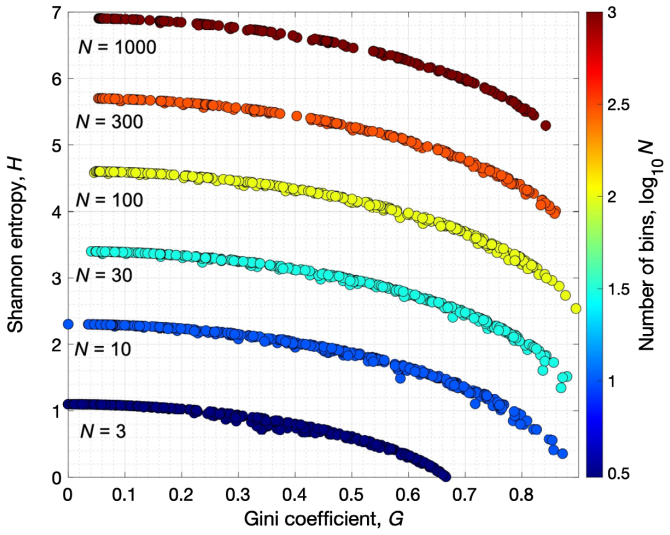

Figure 8. Comparing the Gini coefficient G and Shannon entropy H measures of nonuniformity. The curves show the Gini coefficient G (x axis) in analysis with respect to a constant rate versus Shannon entropy H (y axis) for 2400 synthetic discrete distributions with different number N of bins (color). The entropy H is significantly affected by the number N of bins. The entropy H and clustering G are closely (nonlinearly) related for distributions with the same number of bins. The color version of this figure is available only in the electronic edition.

that do not have this feature, so their identification crucially depends on the used model. The nearest-neighbor declustering used in this work takes a flexible approach to this situation.

The procedure implemented in Zaliapin and Ben-Zion (2020) first tries removing the clustered events responsible for the nonfactorized part of the event rate and then allows a user to select (via the cluster threshold α_0) the probability for a given event from the factorized rate population to be background or clustered. Because at present there is no objective criterion to decide how the factorized rate should be partitioned between the clustered and background populations, alternative declustering techniques can result in substantially different numbers of background events when applied to the same catalog (e.g., van Stiphout *et al.*, 2012). As already mentioned, although there exists a part of seismicity that is clearly clustered and a part that is clearly background, the gray zone between these two subpopulations may be large enough to produce substantially different versions of a "properly" declustered catalog.

The ROC-based clustering measure G is related to the Shannon entropy (Shannon, 1948), which is defined for a distribution $p(i)$ as $H = -\Sigma p(i) \log p(i)$ and has the same informal interpretation: quantifying the degree of nonuniformity. The main difference between the entropy H and clustering G is that the latter is much less affected by the number of bins in the distribution (the total number of voxels in our case). Figure 8 compares the entropy H and clustering G in a synthetic

experiment that produces 400 measures with different degree of nonuniformity for each of the bin counts $N = 3$, 10, 30, 100, 300, and 1000. The entropy and clustering are closely related for each given N. However, the entropy is heavily affected by the number of bins, whereas clustering is not sensitive to this parameter. The two measures have a negative (nonlinear) relation, because G increases and H decreases for a higher degree of nonuniformity. We also observe that H has a weaker discriminating power for low G values, which is reflected in almost zero slopes of the curves in Figure 8 at $G < 0.2$.

The increasing quality of earthquake records and the complexity of problems associated with seismicity require refined and more sophisticated methods for earthquake clustering analyses, because space–time clustering dominate natural earthquake catalogs. Declustered versions of seismicity are needed for various analyses. Until there are accepted solutions for the physics and mathematics behind different forms of earthquake clustering, the used declustering approaches remain intrinsically heuristic and exploratory. Simplicity of implementation and flexibility of output have some advantages at the current stage, but ultimately the appropriate form of the resulting product (declustered catalog) depend on the quality of the full catalog and problem at hand.

Data and Resources

The relocated catalog of Hauksson *et al.* (2012) is available from the Southern California Earthquake Data Center (https://scedc.caltech.edu/data/alt-2011-dd-hauksson-yang-shearer.html) The U.S. Geological Survey (USGS) comprehensive catalog (ComCat) is available at https://earthquake.usgs.gov/data/comcat/. The International Seismological Centre–Global Earthquake Model (ISC-GEM) Earthquake Catalogue is available at doi: 10.31905/d808b825. The epidemic-type aftershock sequence (ETAS) catalog is available in the electronic supplement of Gu *et al.* (2013, doi: 10.1002/jgrb.50306). All websites were last accessed in September 2021. Supplemental material for this article includes a formal definition of the receiver operating characteristic (ROC) diagram and describes stability analysis of the clustering measure G using data from the southern California.

Declaration of Competing Interests

The authors declare no competing interests.

Acknowledgments

The study was supported by the National Science Foundation (NSF; Grants EAR-1723033 and EAR-1722561) and the Southern California Earthquake Center (based on NSF Cooperative Agreement EAR-1600087 and U.S. Geological Survey [USGS] Cooperative Agreement G17 AC00047). This article benefitted from comments by two anonymous reviewers and an anonymous associate editor.

References

Abolfathian, N., P. Martínez-Garzón, and Y. Ben-Zion (2019). Spatiotemporal variations of stress and strain parameters in the San Jacinto fault zone, *Pure Appl. Geophys.* **176,** no. 3, 1145–1168, doi: 10.1007/s00024-018-2055-y.

Amos, C. B., P. Audet, W. C. Hammond, R. Bürgmann, I. A. Johanson, and G. Blewitt (2014). Uplift and seismicity driven by groundwater depletion in central California, *Nature* **509,** no. 7501, 483–486.

Baiesi, M., and M. Paczuski (2004). Scale-free networks of earthquakes and aftershocks, *Phys. Rev. E* **69,** no. 6, 066106, doi: 10.1103/PhysRevE.69.066106.

Ben-Zion, Y. (2008). Collective behavior of earthquakes and faults: Continuum-discrete transitions, evolutionary changes and corresponding dynamic regimes, *Rev. Geophys.* **46,** RG4006, doi: 10.1029/2008RG000260.

Ben-Zion, Y., and I. Zaliapin (2020). Localization and coalescence of seismicity before large earthquakes, *Geophys. J. Int.* **223,** no. 1, 561–583.

Ben-Zion, Y., J. R. Rice, and R. Dmowska (1993). Interaction of the San Andreas fault creeping segment with adjacent great rupture zones, and earthquake recurrence at Parkfield, *J. Geophys. Res.* **98,** no. B2, 2135–2144, doi: 10.1029/92JB02154.

Bettinelli, P., J. P. Avouac, M. Flouzat, L. Bollinger, G. Ramillien, S. Rajaure, and S. Sapkota (2008). Seasonal variations of seismicity and geodetic strain in the Himalaya induced by surface hydrology, *Earth Planet. Sci. Lett.* **266,** 332–344.

Cochran, E. S., J. E. Vidale, and S. Tanaka (2004). Earth tides can trigger shallow thrust fault earthquakes, *Science* **306,** no. 5699, 1164–1166.

Console, R., D. D. Jackson, and Y. Y. Kagan (2010). Using the ETAS model for catalog declustering and seismic background assessment, *Pure Appl. Geophys.* **167,** no. 6, 819–830.

Console, R., M. Murru, and F. Catalli (2006). Physical and stochastic models of earthquake clustering, *Tectonophysics* **417,** nos. 1/2, 141–153.

Dieterich, J. (1994). A constitutive law for rate of earthquake production and its application to earthquake clustering, *J. Geophys. Res.* **99,** no. B2, 2601–2618.

Dieterich, J. H., and D. E. Smith (2009). Nonplanar faults: Mechanics of slip and off-fault damage, in *Mechanics, Structure and Evolution of Fault Zones*, Birkhäuser, Basel, Switzerland, 1799–1815.

Di Giacomo, D., I. Bondár, D. A. Storchak, E. R. Engdahl, P. Bormann, and J. Harris (2015). ISC-GEM: Global instrumental earthquake catalogue (1900–2009), III. Re-computed M_S and m_b, proxy M_W, final magnitude composition and completeness assessment, *Phys. Earth Planet. In.* **239,** 33–47.

Di Giacomo, D., E. R. Engdahl, and D. A. Storchak (2018). The ISC-GEM earthquake catalogue (1904–2014): Status after the extension project, *Earth Syst. Sci. Data* **10,** 1877–1899, doi: 10.5194/essd-10-1877-2018.

Enescu, B., S. Hainzl, and Y. Ben-Zion (2009). Correlations of seismicity patterns in Southern California with surface heat flow data, *Bull. Seismol. Soc. Am.* **99,** no. 6, 3114–3123.

Felzer, K. R., and E. E. Brodsky (2006). Decay of aftershock density with distance indicates triggering by dynamic stress, *Nature* **441,** no. 7094, 735–738.

Field, E. H., K. R. Milner, J. L. Hardebeck, M. T. Page, N. van der Elst, T. H. Jordan, A. J. Michael, B. E. Shaw, and M. J. Werner (2017). A spatiotemporal clustering model for the third Uniform California Earthquake Rupture Forecast (UCERF3-ETAS): Toward an operational earthquake forecast, *Bull. Seismol. Soc. Am.* **107,** no. 3, 1049–1081.

Gardner, J. K., and L. Knopoff (1974). Is the sequence of earthquakes in Southern California, with aftershocks removed, Poissonian? *Bull. Seismol. Soc. Am.* **64,** no. 5, 1363–1367.

Goebel, T. H. W., and E. E. Brodsky (2018). The spatial footprint of injection wells in a global compilation of induced earthquake sequences, *Science* **361,** no. 6405, 899–904, doi: 10.1126/science.aat5449.

Goebel, T. H. W., T. Candela, C. G. Sammis, T. W. Becker, G. Dresen, and D. Schorlemmer (2014). Seismic event distributions and off-fault damage during frictional sliding of saw-cut surfaces with predefined roughness, *Geophys. J. Int.* **196,** no. 1, 612–625.

Gu, C., A. Y. Schumann, M. Baiesi, and J. Davidsen (2013). Triggering cascades and statistical properties of aftershocks, *J. Geophys. Res.* **118,** no. 8, 4278–4295.

Hammond, W. C., C. Kreemer, I. Zaliapin, and G. Blewitt (2019). Drought-triggered magmatic inflation, crustal strain and seismicity near the Long Valley Caldera, Central Walker Lane, *J. Geophys. Res.* **124,** 6072–6091, doi: 10.1029/2019JB017354.

Hauksson, E., W. Yang, and P. M. Shearer (2012). Waveform relocated earthquake catalog for Southern California (1981 to June 2011), *Bull. Seismol. Soc. Am.* **102,** no. 5, 2239–2244, doi: 10.1785/0120120010.

Hsu, Y. J., H. Kao, R. Bürgmann, Y. T. Lee, H. H. Huang, Y. F. Hsu, Y. M. Wu, and J. Zhuang (2021). Synchronized and asynchronous modulation of seismicity by hydrological loading: A case study in Taiwan, *Sci. Adv.* **7,** no. 16, eabf7282, doi: 10.1126/sciadv.abf7282.

Johnson, C. W., Y. Fu, and R. Bürgmann (2019). Hydrospheric modulation of stress and seismicity on shallow faults in southern Alaska, *Earth Planet. Sci. Lett.* **530,** 115904, doi: 10.1016/j.epsl.2019.115904.

Jones, L. M., and P. Molnar (1979). Some characteristics of foreshocks and their possible relationship to earthquake prediction and premonitory slip on faults, *J. Geophys. Res.* **84,** no. B7, 3596–3608.

Kagan, Y. Y. (2003). Accuracy of modern global earthquake catalogs, *Phys. Earth Planet. In.* **135,** nos. 2/3, 173–209.

Kagan, Y. Y., and D. D. Jackson (1991). Long-term earthquake clustering, *Geophys. J. Int.* **104,** no. 1, 117–133.

Kagan, Y. Y., and D. D. Jackson (2000). Probabilistic forecasting of earthquakes, *Geophys. J. Int.* **143,** no. 2, 438–453.

Kato, A., and Y. Ben-Zion (2021). The generation of large earthquakes, *Nat. Rev. Earth Environ.* **2,** 26–39, doi: 10.1038/s43017-020-00108-w.

Knopoff, L. (1964). The statistics of earthquakes in Southern California, *Bull. Seismol. Soc. Am.* **54,** no. 6A, 1871–1873.

Knopoff, L. (2000). The magnitude distribution of declustered earthquakes in Southern California, *Proc. Natl. Acad. Sci. Unit. States Am.* **97,** no. 22, 11,880–11,884.

Lengliné, O., B. Enescu, Z. Peng, and K. Shiomi (2012). Decay and expansion of the early aftershock activity following the 2011, M_w 9.0 Tohoku earthquake, *Geophys. Res. Lett.* **39,** L18309, doi: 10.1029/2012GL052797.

Llenos, A. L., and A. J. Michael (2020). Regionally optimized background earthquake rates from ETAS (ROBERE) for probabilistic seismic hazard assessment, *Bull. Seismol. Soc. Am.* **110,** 1172–1190, doi: 10.1785/0120190279.

Luen, B., and P. B. Stark (2012). Poisson tests of declustered catalogues, *Geophys. J. Int.* **189,** no. 1, 691–700, doi: 10.1111/j.1365-246X.2012.05400.x.

Marsan, D., and O. Lengline (2008). Extending earthquakes' reach through cascading, *Science* **319,** no. 5866, 1076–1079, doi: 10.1126/science.1148783.

Martínez-Garzón, P., Y. Ben-Zion, N. Abolfathian, G. Kwiatek, and M. Bohnhoff (2016). A refined methodology for stress inversions of earthquake focal mechanisms, *J. Geophys. Res.* **121,** 8666–8687, doi: 10.1002/2016JB013493.

Martínez-Garzón, P., V. Vavryčuk, G. Kwiatek, and M. Bohnhoff (2016). Sensitivity of stress inversion of focal mechanisms to pore pressure changes, *Geophys. Res. Lett.* **43,** no. 16, 8441–8450.

Michael, A. J. (1987). Use of focal mechanisms to determine stress: A control study, *J. Geophys. Res.* **92,** no. B1, 357–368.

Michael, A. J. (2014). How complete is the ISC-GEM global earthquake catalog? *Bull. Seismol. Soc. Am.* **104,** no. 4, 1829–1837.

Mignan, A. (2014). The debate on the prognostic value of earthquake foreshocks: A meta-analysis, *Sci. Rep.* **4,** no. 1, 1–5.

Mizrahi, L., S. Nandan, and S. Wiemer (2021). The effect of declustering on the size distribution of mainshocks, *Seismol. Res. Lett.* **92,** no. 4, 2333–2342, doi: 10.1785/0220200231.

Ogata, Y. (1999). Seismicity analysis through point-process modeling: A review, in *Seismicity Patterns, Their Statistical Significance and Physical Meaning*, 471–507.

Peresan, A., and S. Gentili (2020). Identification and characterisation of earthquake clusters: A comparative analysis for selected sequences in Italy and adjacent regions, *Boll. Geofis. Teor. Appl.* **16,** no. 2, doi: 10.4430/bgta0249.

Petersen, M. D., M. P. Moschetti, P. M. Powers, C. S. Mueller, K. M. Haller, A. D. Frankel, Y. Zeng, S. Rezaeian, S. C. Harmsen, O. S. Boyd, *et al.* (2015). The 2014 United States national seismic hazard model, *Earthq. Spectra* **31,** 1_suppl, S1–S30, doi: 10.1193/120814EQS210M.

Petersen, M. D., C. S. Mueller, M. P. Moschetti, S. M. Hoover, K. S. Rukstales, D. E. McNamara, R. A. Williams, A. M. Shumway, P. M. Powers, P. S. Earle, *et al.* (2018). 2018 one-year seismic hazard forecast for the Central and Eastern United States from induced and natural earthquakes, *Seismol. Res. Lett.* **89,** no. 3, 1049–1061, doi: 10.1785/0220180005.

Pollitz, F. F., R. Bürgmann, R. S. Stein, and V. Sevilgen (2014). The profound reach of the 11 April 2012 M 8.6 Indian Ocean earthquake: Short-term global triggering followed by a longer-term global shadow, *Bull. Seismol. Soc. Am.* **104,** no. 2, 972–984, doi: 10.1785/0120130078.

Powers, P. M., and T. H. Jordan (2010). Distribution of seismicity across strike-slip faults in California, *J. Geophys. Res.* **115,** no. B5, doi: 10.1029/2008JB006234.

Press, F., and C. Allen (1995). Patterns of seismic release in the southern California region, *J. Geophys. Res.* **100,** no. B4, 6421–6430.

Reasenberg, P. (1985). Second-order moment of central California seismicity, 1969–1982, *J. Geophys. Res.* **90,** 5479–5496.

Ross, Z. E., and E. S. Cochran (2021). Evidence for latent crustal fluid injection transients in Southern California from long-duration earthquake swarms, *Geophys. Res. Lett.* **48,** no. 12, e2021GL092465.

Ross, Z. E., C. Rollins, E. S. Cochran, E. Hauksson, J.-P. Avouac, and Y. Ben-Zion (2017). Aftershocks driven by afterslip and fluid pressure sweeping through a fault-fracture mesh, *Geophys. Res. Lett.* **44,** 8260–8267, doi: 10.1002/2017GL074634.

Ross, Z. E., D. T. Trugman, E. Hauksson, and P. M. Shearer (2019). Searching for hidden earthquakes in Southern California, *Science* **364,** no. 6442, 767–771.

Rosson, Z., J. I. Walter, T. Goebel, and X. Chen (2019). Narrow spatial aftershock zones for induced earthquake sequences in Oklahoma, *Geophys. Res. Lett.* **46,** 10,358–10,366, doi: 10.1029/2019gl083562.

Ruhl, C. J., R. E. Abercrombie, K. D. Smith, and I. Zaliapin (2016). Complex spatiotemporal evolution of the 2008 M_w 4.9 Mogul earthquake swarm (Reno, Nevada): Interplay of fluid and faulting, *J. Geophys. Res.* **121,** no. 11, 8196–8216.

Schoenberg, F. P. (2013). Facilitated estimation of ETAS, *Bull. Seismol. Soc. Am.* **103,** no. 1, 601–605.

Seif, S., A. Mignan, J. D. Zechar, M. J. Werner, and S. Wiemer (2017). Estimating ETAS: The effects of truncation, missing data, and model assumptions, *J. Geophys. Res.* **122,** no. 1, 449–469.

Shannon, C. E. (1948). A mathematical theory of communication, *Bell Syst. Tech. J.* **27,** no. 3, 379–423.

Shcherbakov, R. (2020). Statistics and forecasting of aftershocks during the 2019 Ridgecrest, California, earthquake sequence, *J. Geophys. Res.* **126,** no. 2, e2020JB020887.

Storchak, D. A., D. Di Giacomo, I. Bondár, E. R. Engdahl, J. Harris, W. H. K. Lee, A. Villaseñor, and P. Bormann (2013). Public release of the ISC-GEM global instrumental earthquake catalogue (1900-2009), *Seismol. Res. Lett.* **84,** no. 5, 810–815, doi: 10.1785/0220130034.

Storchak, D. A., D. Di Giacomo, E. R. Engdahl, J. Harris, I. Bondár, W. H. K. Lee, P. Bormann, and A. Villaseñor (2015). The ISC-GEM global instrumental earthquake catalogue (1900-2009): Introduction, *Phys. Earth Planet. In.* **239,** 48–63, doi: 10.1016/j.pepi.2014.06.009.

Taroni, M., and A. Akinci (2021). Good practices in PSHA: Declustering, *b*-value estimation, foreshocks and aftershocks inclusion; a case study in Italy, *Geophys. J. Int.* **224,** no. 2, 1174–1187.

Teng, G., and J. W. Baker (2019). Seismicity declustering and hazard analysis of the Oklahoma-Kansas region, *Bull. Seismol. Soc. Am.* **109,** 2356–2366, doi: 10.1785/0120190111.

Uhrhammer, R. (1986). Characteristics of Northern and Central California seismicity, *Earthq. Notes* **57,** no. 1, 21.9.

Utsu, T. (1970). Aftershocks and earthquake statistics I, *J. Fac. Sci.* **3,** 129–195, Hokkaido University of Geophysics.

Utsu, T. (2002). Statistical features of seismology, in *International Handbook of Earthquake and Engineering Seismology, Part A*, W. H. K. Lee, H. Kanamori, P. C. Jennings, and C. Kisslinger (Editors), Academic Press, 719–732.

Utsu, T., and Y. Ogata (1995). The centenary of the Omori formula for a decay law of aftershock activity, *J. Phys. Earth* **43,** no. 1, 1–33.

van der Elst, N. J. (2017). Accounting for orphaned aftershocks in the earthquake background rate, *Geophys. J. Int.* **211,** no. 2, 1108–1118.

van Stiphout, T., D. Schorlemmer, and S. Wiemer (2011). The effect of uncertainties on estimates of background seismicity rate, *Bull. Seismol. Soc. Am.* **101,** no. 2, 482–494.

van Stiphout, T., J. Zhuang, and D. Marsan (2012). Seismicity declustering, *Community Online Resource for Statistical Seismicity Analysis*, doi: 10.5078/corssa-52382934.

Varini, E., A. Peresan, and J. Zhuang (2020). Topological comparison between the stochastic and the nearest-neighbor earthquake declustering methods through network analysis, *J. Geophys. Res.* **125,** no. 8, e2020JB019718, doi: 10.1029/2020JB019718.

Vavryčuk, V. (2014). Iterative joint inversion for stress and fault orientations from focal mechanisms, *Geophys. J. Int.* **199,** no. 1, 69–77.

Veen, A., and F. P. Schoenberg (2008). Estimation of space–time branching process models in seismology using an EM–type algorithm, *J. Am. Stat. Assoc.* **103,** no. 482, 614–624.

Wang, Q., D. D. Jackson, and J. Zhuang (2010). Missing links in earthquake clustering models. *Geophys. Res. Lett.* **37,** no. 21, doi: 10.1029/2010GL044858.

Wang, Q., F. P. Schoenberg, and D. D. Jackson (2010). Standard errors of parameter estimates in the ETAS model, *Bull. Seismol. Soc. Am.* **100,** no. 5A, 1989–2001.

Wasserman, L. (2006). *All of Nonparametric Statistics*, Springer Science & Business Media, New York, New York, 282 pp.

Woessner, J., S. Hainzl, W. Marzocchi, M. J. Werner, A. M. Lombardi, F. Catalli, B. Enescu, M. Cocco, M. C. Gerstenberger, and S. Wiemer (2011). A retrospective comparative forecast test on the 1992 Landers sequence, *J. Geophys. Res.* **116,** no. B5, doi: 10.1029/2010JB007846.

Zaliapin, I., and Y. Ben-Zion (2013). Earthquake clusters in southern California I: Identification and stability, *J. Geophys. Res.* **118,** no. 6, 2847–2864.

Zaliapin, I., and Y. Ben-Zion (2015). Artefacts of earthquake location errors and short-term incompleteness on seismicity clusters in southern California, *Geophys. J. Int.* **202,** no. 3, 1949–1968.

Zaliapin, I., and Y. Ben-Zion (2016). A global classification and characterization of earthquake clusters, *Geophys. J. Int.* **207,** no. 1, 608–634.

Zaliapin, I., and Y. Ben-Zion (2020). Earthquake declustering using the nearest-neighbor approach in space-time-magnitude domain, *J. Geophys. Res.* **125,** no. 4, e2018JB017120, doi: 10.1029/2018JB017120.

Zaliapin, I., A. Gabrielov, V. Keilis-Borok, and H. Wong (2008). Clustering analysis of seismicity and aftershock identification, *Phys. Rev. Lett.* **101,** no. 1, 018501, doi: 10.1103/PhysRevLett.101.018501.

Zeng, Y., M. D. Petersen, and Z.-K. Shen (2018). Earthquake potential in California-Nevada implied by correlation of strain rate and seismicity, *Geophys. Res. Lett.* **45,** 1778–1785.

Zhuang, J., Y. Ogata, and D. Vere-Jones (2002). Stochastic declustering of space-time earthquake occurrences, *J. Am. Stat. Assoc.* **97,** no. 458, 369–380, doi: 10.1198/016214502760046925.

Manuscript received 17 May 2021
Published online 22 September 2021